Synthesis, Characterization and Photocatalytic Behavior of SiO_2@nitrized-TiO_2 Nanocomposites Obtained by a Straightforward Novel Approach

Antonino Gulino,[b] Georgia Papanikolaou,[a] Paola Lanzafame,[a] Abdellatif Aaliti,[c] Patrizia Primerano,[d] Luca Spitaleri,[b] Claudia Triolo,[e] Zainab Dahrouch,[c] Amani Khaskhoussi,[d] and Sandra Lo Schiavo*[a]

We report on the facile synthesis of SiO_2@nitrized-TiO_2 nanocomposite (NST) by calcination of TiO_2 xerogel with OctaAmmonium POSS® (N-POSS; POSS = polyhedral oligomeric silsesquioxanes). The as-obtained nanoporous mixed oxide is constituted by uniformly distributed SiO_2 and nitrized-TiO_2, where the silica component is present in an amorphous state and TiO_2 in an anatase/rutile mixed phase (92.1% vs. 7.9%, respectively) with very small anatase crystallites (3.7 nm). The TiO_2 lattice is nitrized both at interstitial and substitutional positions. NST features a negatively charged surface with a remarkable surface area (406 $m^2 g^{-1}$), endowed with special adsorption capabilities towards cationic dyes. Its photocatalytic behavior was tested by following the degradation of standard aqueous methylene blue and methyl orange solutions under UV and visible light irradiation, according to ISO 10678:2010. For comparison, analogous investigations were carried out on a silica-free N–TiO_2, obtained by using NH_4Cl as nitrogen source.

1. Introduction

Nano-TiO_2 based materials are the most widely investigated semiconductor photocatalysts due to their potential application in fuel production and environmental remediation.[1] They offer unique advantages in terms of physical and chemical stability, low cost, low toxicity, high redox potential and tunable optoelectronic properties. They are largely applied, among others, as materials for self-cleaning antibacterial coatings, antifogging mirrors, water and air purification as well as for solar cells.[1,2]

Several strategies have been developed in order to increase the photocatalytic efficiency and stability of such systems. This includes engineering of heterojunction, mixed oxides and doping aimed to obtain morphological (large surface area, porosity etc.) and/or electronic modifications.

Degussa P25, the most popular and commercially available nano-TiO_2 system, is a representative example of biphasic interfacial heterojunction structure, (anatase-rutile composition = 70:30) exhibiting a superior activity compared to pure anatase. Thanks to its lower E_g, rutile generates electrons which move from the rutile conduction band to "the trapping sites of anatase surface", slowing down the electron-hole recombination process .[3–5]

Narrowing of the TiO_2 band gap to access visible light-activated (VLA) materials may be reached by metal doping, co-doping, surface modification by metal complexes, organic dyes and coupling of semiconductors.[3–5] However, the most pursued strategy of access to VLA TiO_2 photocatalysts includes the use of non-metal systems (usually referred as generation II), nitrogen-based systems representing the most investigated ones.[6–9]

SiO_2@TiO_2 nanocomposites, freestanding or combined with other materials (oxides, metal atoms, polymers, mortars, etc.) are among the most investigated mixed oxides. The presence of SiO_2 infers an increased surface area and, in turn, special adsorption properties towards water, dyes and pollutants to these systems, which were largely exploited for the implementation of multi-contaminated water/wastewater remediation processes.[10–17] This also affects their photocatalytic performance, as the accumulation of water and hydroxyl groups on the photocatalytic surface constitutes a fundamental step of the

[a] Prof. Dr. G. Papanikolaou, Prof. Dr. P. Lanzafame, Prof. Dr. S. Lo Schiavo
Department of Chemical, Biological, Pharmaceutical and Environmental Sciences
University of Messina
Viale F. Stagno d'Alcontres, 31, 98166 Messina (Italy)
E-mail: sloschiavo@unime.it
[b] Prof. Dr. A. Gulino, Prof. Dr. L. Spitaleri
Department of Chemical Sciences
University of Catania, and INSTM UdR of Catania
Viale Andrea Doria 6, 95125 Catania (Italy)
[c] Prof. Dr. A. Aaliti, Z. Dahrouch
Département de Génie Chimique, Laboratoire Physico-Chimie des Matériaux, Substances Naturelles et Environnement
Faculté des Sciences et Techniques de Tanger
Ancienne Route de l'Aéroport, Km 10, Ziaten. BP: 416. Tanger (Maroc)
[d] Prof. Dr. P. Primerano, A. Khaskhoussi
Dipartimento di Ingegneria
Università degli Studi di Messina
Contrada Di Dio, 98166 Messina (Italy)
[e] Prof. Dr. C. Triolo
Dipartimento di Ingegneria Civile, dell'Energia, dell'Ambiente e dei Materiali (DICEAM)
Università "Mediterranea"
Via Graziella, Loc. Feo di Vito, 89122 Reggio Calabria (Italy)

Supporting information for this article is available on the WWW under https://doi.org/10.1002/open.202100157

whole photocatalytic cycle. The presence of SiO_2 also plays an important role in determining superior physical properties (textural, thermal, mechanical), reduced TiO_2 size and self-agglomeration of TiO_2 nanoparticles.

Diversified procedures have been employed for the building of SiO_2@TiO_2 mixed nano-oxides such as sol-gel, hydrothermal, solid-mixing, hetero-coagulation, just to name the most common.[10–19]

Ionic Liquids (ILs), that is, organic salts melting below 100 °C, have become a "major subject of study for modern chemistry due to their high potential of applications in many industrial fields".[20–23] The chemical versatility of ILs stems from their ionic nature which, by a proper selection of the cation–anion ion pair, allows a synthetic control of their functions, such as thermal stability, negligible low vapor pressure, electric conductivity, solvent properties and bioactivity.[24–30] Due to their low vapor pressure, ILs are commonly used as alternative, "green" solvents to conventional organic media in chemical synthesis, catalysis, separation processes, biomass processing, electrochemistry and nano- and bio-technologies.[31–33]

ILs, among others, have been widely exploited as directing and capping agents for the synthesis of TiO_2 nanomaterials with controlled morphologies and enhanced photoactivity.[31–33]

Our interest in polyhedral oligomeric silsesquioxanes (POSS) salts/ILs leads us to focus our attention on POSS bearing ammonium substituents,[34–37] as species that can act as nano-silica source and directing agents in the building of SiO_2@TiO_2 mixed nano-oxides. POSS, in brief, are a versatile class of nanohybrids featured by a cube-shaped siloxane nano-scaffold $(SiO_{1.5})_x$ surrounded by organic substituents, which may be inert or functionalized.[38–42] For the purposes of our project, star-shaped POSS-ammonium salts/ILs have been selected. It is expected that, by modifying their structure, that is, by introducing alkyl chains of different lengths on ammonium moieties and/or by varying the nature of the anion,[35] SiO_2@TiO_2 nanocomposites with different textural properties, morphologies and activities can be obtained.[43–45]

Therefore, we report here on the straightforward synthesis of SiO_2@nitrized-TiO_2 nanocomposite (NST) by calcination of TiO_2 "xerogel" and OctaAmmonium POSS® (N-POSS, Figure 1) mixture. The new material has been characterized by XRD, Raman, SEM, IR, XPS and N_2 physisorption measurements. Photoactivity tests have been carried out by using methylene blue (MB) (ISO10678:2010, Geneva-2010) and methyl orange (MO) as cationic and anionic dye degradation models, respectively.

We anticipate that such a strategy leads to a significant nitrization of TiO_2 nanoparticles. Consistently, comparative photocatalytic tests and investigations were also performed on a free-silica N-doped TiO_2 sample (NT), prepared by using NH_4Cl as N-doping agent.

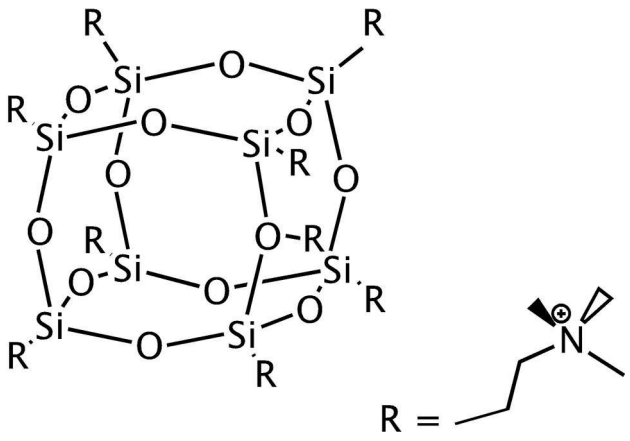

Figure 1. Schematic representation of OctaAmmonium POSS®.

2. Results and Discussion

2.1. X-Ray Diffraction

The phase and crystallinity of NST were characterized by X-ray diffraction spectroscopy (XRD). The XRD pattern of NST is shown in Figure 2, along with that of the free-silica NT and the commercial TiO_2 Degussa P25, the latter consisting of anatase and rutile crystalline phases in a ratio of about 3:1.[46]

No signals related to crystalline silica were observed in the diffractogram, thus suggesting that, upon annealing, the POSS ionic reactant evolves to an amorphous state. According to literature data, amorphous silica may afford a broad signal in the range of $2\theta = 21–23°$.[16] However, this band is often absent in the XRD of SiO_2@TiO_2 nanocomposites.[10–19] The signals attributable to TiO_2, although very broad compared to NT and commercial P25, are consistent with crystallites in anatase/rutile mixed phase. By applying the Scherrer equation, crystallite sizes values of 3.7 nm and 10.5 nm have been obtained for NST and NT, respectively.

The XRD peak broadening found in the NST diffractogram with respect to NT and P25 may be conveniently explained in terms of crystallite sizes as the smaller nanoparticles the broader the signal. In principle, it cannot be excluded the role of amorphous SiO_2 in producing overlapped signals. Never-

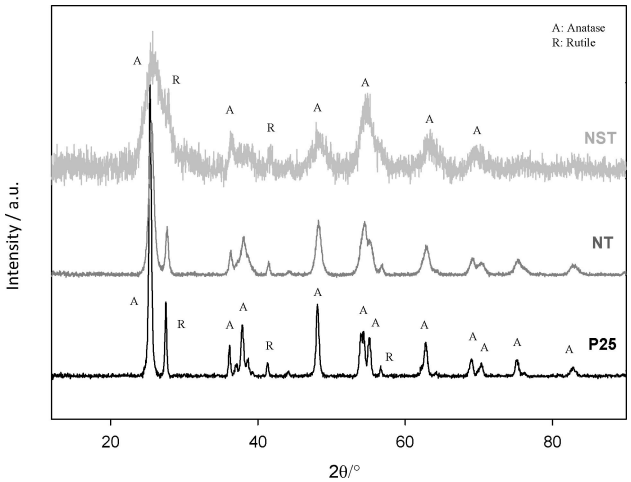

Figure 2. XRD patterns of NST, NT and Degussa P25, where A and R indicate the anatase and rutile phase, respectively.

theless, the peaks are well observable, indicating that most of TiO_2 NPs photocatalyst is present on the material surface.[16,47,48]

2.2. Raman Spectroscopy

The TiO_2 crystalline phase composition of NST and NT samples was also studied by micro-Raman analysis. The Raman spectrum of NST, together with the results of the fitting procedure, is shown in Figure 3, while that of NT is reported in Figure S1 (Supporting Information).[49,50] The anatase and rutile phases possess a tetragonal crystal structure and belong to the space groups D_{4h}^{19} and D_{4h}^{14}, respectively, and usually exhibit Raman active modes in the 100–900 cm^{-1} frequency region. For anatase, optical modes with normal vibrations are: $1A_{1g}+1A_{2u}+2B_{1g}+1B_{2u}+3E_g+2E_u$, of which only six are Raman active: $1A_{1g}+2B_{1g}+3E_g$.[51,52] For the rutile phase, the vibration modes are: $1A_{1g}+1A_{2g}+1A_{2u}+1B_{1g}+1B_{2g}+2B_{1u}+1E_g+3E_u$, of which only B_{1g}, E_g, A_{1g} and B_{2g} are Raman active.[51,52] The Raman spectrum was fitted using a Gaussian function to describe almost all peaks, but a Voigt function to fit the $E_g(1–2)$ band ($\nu=150\ cm^{-1}$) of the anatase phase. We also attribute the peaks $B_{1g}(1)$ at $\nu=400\ cm^{-1}$, $B_{1g}(2)-A_{1g}$ (unresolved) at $\nu=522\ cm^{-1}$ and $E_g(3)$ at $\nu=640\ cm^{-1}$ to anatase. The other two peaks E_g at $\nu=450\ cm^{-1}$ and A_{1g} at $\nu=604\ cm^{-1}$ have been attributed to the rutile phase. To determine the percentage of the two crystalline phases, we evaluated the integrated area of all bands. For each curve, the percentages were calculated as follows [Eqs. (1) and (2)]:

$$A(\%) = \frac{A_{Anatase\ bands}}{A_{total}} * 100 \quad (1)$$

$$R(\%) = \frac{A_{Rutile\ bands}}{A_{total}} * 100 \quad (2)$$

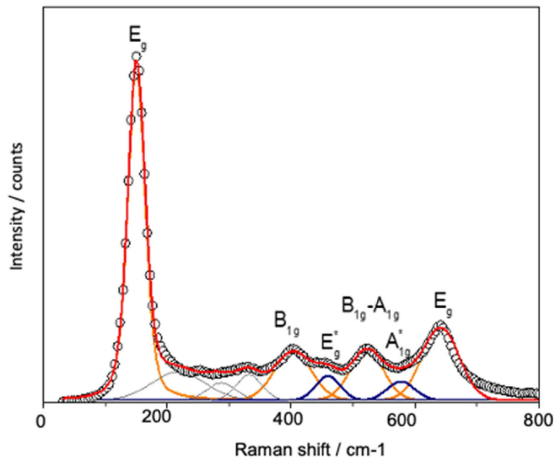

Figure 3. Raman spectrum of NST, where the empty circles represent the experimental data, the red line is the sum of all the Gaussian components as a result of the fitting procedure that reproduces the measured spectral profiles, orange and blue lines indicate the Raman bands attributed to the Anatase and Rutile phases, respectively.

where $A_{Anatase\ bands}$ is the sum of the integrated area of the Raman bands attributed to the anatase phase, $A_{Rutile\ bands}$ is the sum of the integrated area of the Raman bands attributed to the rutile phase, and A_{total} represents the sum of all bands used to fit the Raman spectra.

As a result, NST consists of A = 92.10% and R = 7.9%. Moreover, the Raman spectrum shows a significant shift and a broadening of the lowest frequency E_g symmetry Raman mode with respect to bulk anatase. Both these effects can be attributed to a three-dimensional phonon confinement.[52] Comparable values, A = 86.36% and R = 13.14%, respectively, have been calculated for the NT silica-free sample (Figure S1). Concerning the symmetry of the SiO_2@TiO_2 mixed oxide, we observe that, as reported in literature,[53–55] the transverse-optical modes of the Si–O–Si groups visible in amorphous silica, are placed at ≈460 cm^{-1}, ≈800 cm^{-1}, and ≈1070 cm^{-1}. Among them, the first one is superimposed to the intense B_{1g} Raman mode of the rutile phase, while the last ones fall out the investigated spectral range. Hence, only the background signal, ranging between 200–350 cm^{-1}, can be attributed to SiO_2.This signal is clearly visible in the Raman spectra; however, it is not sufficient for any quantification or qualification.

2.3. SEM Micrographs

The morphology of the as-synthesized NST catalyst was studied by SEM investigations (Figure S2). Figure 4 shows the Energy Dispersive Spectroscopy (EDS) maps for the Si and Ti atoms, respectively. The results point out that these atoms are homogeneously and uniformly distributed in the nanocomposite, with a high amount of N (5.2%) as evidenced by elemental analysis performed by EDX measurements (Figure S3).

2.4. X-Ray Photoelectron Spectroscopy

XP spectra of NST are collected in Figure 5. For comparison also those related to NT and not annealed N-POSS@TiO_2 are reported. All samples show a C 1s peak at 285.0 eV, currently used to calibrate XP spectra.[56,57]

The XP spectra in the C 1s energy region are shown in Figure 5A. The XPS relative intensities are consistent with the related atomic concentration analyses and show that annealing

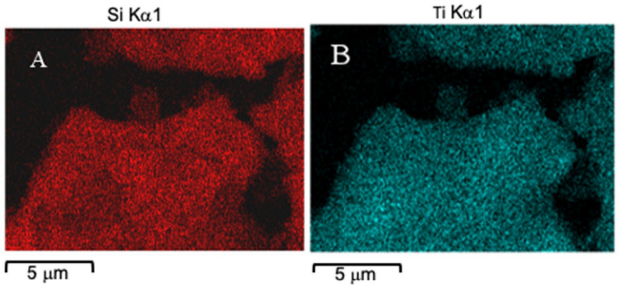

Figure 4. NST EDS mapping of A) silicon and B) titanium, respectively.

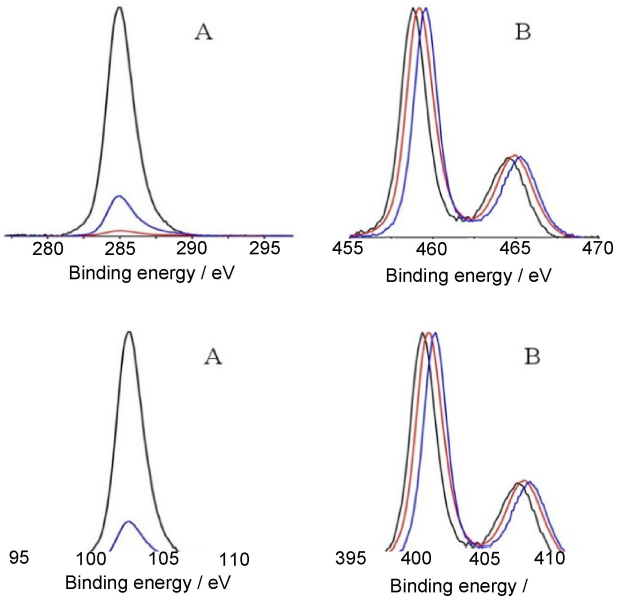

Figure 5. Al Kα excited XPS of N-POSS@TiO_2 (black line), NT (red line) and NST (blue line) measured (A) in the C 1s binding energy region, (B) in the Ti 2p binding energy region, (C) in the Si 2p binding energy region and (D) in the N 1s binding energy region, respectively. Structures due to satellite radiations have been subtracted from the spectra.

at 400 °C (red and blue lines) strongly reduces both the surface adventitious carbon contamination as well as the aliphatic carbon of the POSS system. No carbon dopant has been found in any of the present samples since substituted carbon in C-doped TiO_2 should show a peak at 281.8 eV, absent in our measurements.[58]

Figure 5B shows the XP spectrum in the Ti 2p energy region. The NT sample shows the typical $Ti2p_{1/2,3/2}$ spin-orbit components at 459.1 eV and 464.9 eV, with a 5.8 eV spin–orbit separation. The obtained values are in agreement with a prevalence of the anatase phase.[59–61] The XPS of non-annealed N-POSS@TiO_2 shows a 0.4 eV lower binding energy shift of both spin-orbit components, whilst the annealing procedure causes an opposite behavior, being both Ti 2p spin-orbit components at 0.4 eV higher binding energy.

The high-resolution Si 2p XPS are shown in Figure 5C. The Si 2p states appear at 102.4 eV and 103.1 eV, respectively. Again, the annealing procedure strongly affects the binding energies and the final XPS value (103.1 eV) is consistent with the value expected for the SiO_2 phase.[60]

As a general feature, all the O 1s (Figure S4), Ti 2p and Si 2p states appear ~0.7 eV shifted at higher binding energy upon annealing. The rationalization of this behavior can be achieved by studying the XPS of the N 1s states for all three samples (Figure 4D).

Nitrogen in the anatase lattice of TiO_2 can be interstitial or substitutional. The energy position of N 1s for TiO_2 with N-doped ions located at the substitutional sites was found at 396.8 eV whilst the N 1s peak at ≈400 eV is typically assigned to the interstitial nitrogen dopant (Figure 5D). Only one clear band is observed at 400.2 eV and this is strongly in agreement with the presence of interstitial nitrogen in TiO_2.[58–61] In contrast, the XPS of the non-annealed N-POSS@TiO_2 shows three evident signals at 400.2 eV, 401.5 eV and 406.9 eV. The first peak is due to the above-mentioned interstitial nitrogen. The second peak at 401.5 eV, in tune with a large crop of literature data, is due to the quaternized nitrogen of the POSS system[62–64] and, finally, the last high energy peak is due to some evident nitrates, whose origin has to be found on the adopted synthetic procedure. The annealing at 400 °C (NST sample) causes the disappearing of both nitrates and quaternized nitrogen. Therefore, it seems that annealing of these oxides in presence of nitrates causes some oxidation that finds evidence in the high energy shift of the O 1s, Ti 2p and Si 2p signals, being these final values strongly consistent with those expected for SiO_2 and anatase TiO_2.[59–63]

2.5. Infrared Spectroscopy

FTIR spectra of the non-annealed N-POSS@TiO_2, NT and NST samples are shown in Figure 6. For all samples, it is possible to notice a broad band centered at about 3400 cm^{-1}, associated with the fundamental stretching vibrations of hydroxyl groups of water on the SiO_2 and TiO_2 surfaces. In both N-POSS@TiO_2 and NTS samples, the combination of the Si–O vibrational modes appears at 1636 cm^{-1} and 1382 cm^{-1}.[65,66] The last band becomes very weak after the annealing, as already observed for the thermal degradation of polyhedral oligomeric silsesquioxanes.[67] The weak peak at 1232 cm^{-1}, evident only in the N-POSS@TiO_2 spectrum is related to the vibrations of C–N groups of POSS.[65,66] The broad band in the 500–900 cm^{-1} range is consistent with stretching vibrations such as Ti–O and O–Ti–O.[62,64] The additional broad band in the 870–1190 cm^{-1} range, absent in the NT spectrum, is attributed to asymmetric Si–OH, Si–O–Si and Si–O–Ti vibrations.[65,66] In more detail, the bands at higher wavenumbers (1000–1100 cm^{-1}) are typical of three-dimensional asymmetric Si–O–Si stretching vibrations,

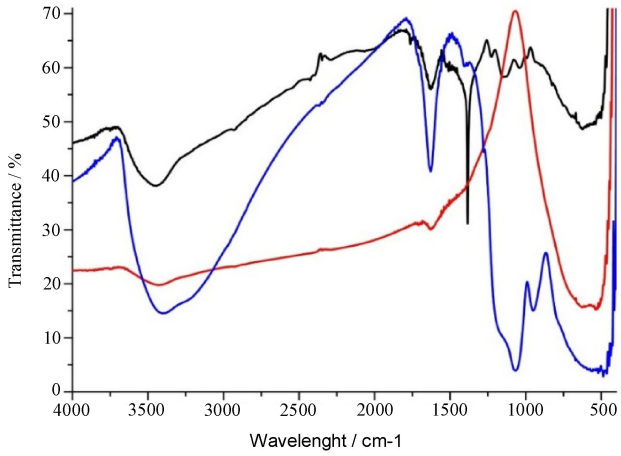

Figure 6. FTIR spectra of NST (blue line), NT (red line) and non-annealed N-POSS@TiO_2 (black line), measured in the 4000–400 cm^{-1} wavelength range.

while that centered at 945 cm^{-1} may be ascribed to Si–O–Ti.[68,69]

2.6. Textural Properties

The textural properties of NST were investigated by N_2 physisorption measurements at −196 °C. The N_2 adsorption-desorption isotherms of the NST sample, together with that of NT, are reported in Figure 7. According to IUPAC classification, the NST sample shows a combination of I-type IV isotherms indicative of a micro-mesoporous material. Moreover, it presents a H4 hysteresis loop in the adsorption-desorption isotherm for $p/p_0 > 0.4$, consistent with the presence of pores with a narrow slit shape.[70,71] The NT sample shows a type IV isotherm typical of a mesoporous material.

Compared to the as-synthesized NT, which presents a BET surface area of above 51 $m^2 g^{-1}$, the presence of silica in NST nanocomposite leads to a significant increase of the BET surface area, reaching a remarkable value of 406 $m^2 g^{-1}$. As shown in Table 1, NST presents a pore volume of 0.223 $cm^3 g^{-1}$ with an average pore diameter of 2.6 nm.

2.7. Photocatalytic activity

The photocatalytic activity of NST was tested by irradiating $1 \cdot 10^{-5}$ M aqueous solutions of the cationic MB and anionic MO test species, respectively. Analogous tests were performed for the free-silica NT sample. Measurements were performed by monitoring the absorbance peak of MB and MO at 662 nm and 475 nm, respectively. The experiments were carried out both under UV (300 nm) and visible (550 nm) light, at increasing irradiation times. Figure 8 reports the relative absorbance $log(A/A_0)$ as function of the time (t), where A and A_0 are the absorbances measured at t and t = 0 s, respectively. The experimental data have been fitted by the Langmuir–Hinshelwood equation [Eq. (3)]:[72]

$$log\left(\frac{A}{A_0}\right) = -k_\alpha . t \quad (3)$$

Where the rate constant k_α is given by the slope of the plots $log(A/A_0)$ versus the irradiation time.

The MB solution, after equilibration in the dark (see Experimental Section), displays a high decrease in concentration (80 %), indicating that an adsorption process takes place on the catalyst surface which, in turn, appears turquoise/green. No significant adsorption changing is observable for NT, suggesting that the adsorption of the cationic MB dye is driven by SiO_2.[13,18]

As shown in Figure 8A, under UV light exposure, NST induces an abrupt reduction of the MB concentration, with a photodegradation rate of 0.017 min^{-1} comparable with that of NT (0.015 min^{-1}). It is to underline that, after UV irradiation, the NST surface catalyst still appeared colored. To have a better insight on this finding, the photocatalyst was recovered, washed repeatedly with water and reused in a new photocatalytic cycle. The as-obtained photodegradation rate (0.018 min^{-1}) differs very slightly from that previously obtained,

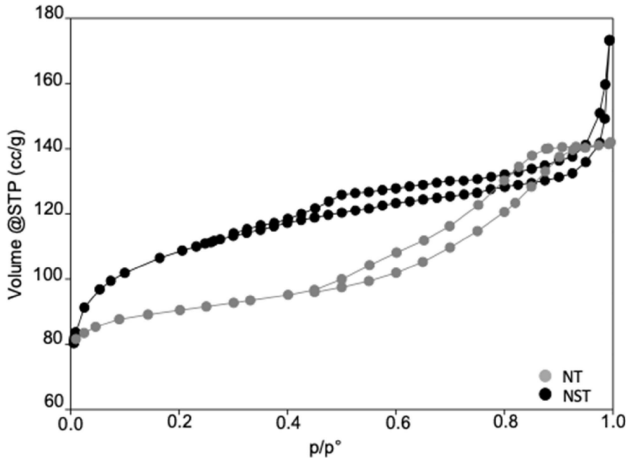

Figure 7. N_2 adsorption-desorption isotherms of NT and NST samples.

Table 1. Textural properties of NST and NT samples.

Sample	S.A.$_{BET}$ [$m^2 g^{-1}$]	S_{micro} [$m^2 g^{-1}$]	$V_{pore\ (BJH\ Adsorption)}$ [$cm^3 g^{-1}$]	Average pore Diameter [nm]
NT	51	n.a.	0.106	8.2
NST	406	319	0.223	2.6

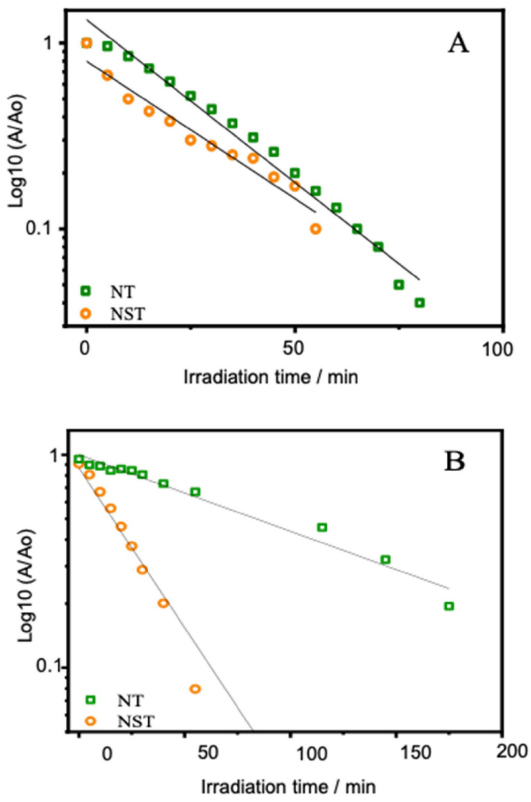

Figure 8. Semi logarithmic plot of A/A_0 as a function of the irradiation time for (A) MB and (B) MO degradation under UV radiation.

indicating that the SiO_2 adsorption active sites do not contribute to the overall photoactivity process of NST.

Instead, under visible irradiation (Figure S6), NST experiences a lower photoactivity, for which a degradation constant of 0.0016 min^{-1} was measured, remarkably smaller than that of the NT silica-free sample (0.015 min^{-1}).

Unlike what observed with MB, NST shows a slighter adsorption activity versus the anionic MO dye compared to MB. After equilibration in the dark, only a 10% reduction in concentration was found. No adsorption of MO was observed for NT. The MO relative absorbance as a function of UV irradiation time is reported in Figure 8B. The results highlight that the UV photoactivity of NST is much higher than that of the free-silica NT sample, the measured degradation constant amounting to 0.015 min^{-1} and 0.0035 min^{-1}, respectively. The data obtained by Vis irradiation (Figure S7) reports a diametral result as the photoactivity of NT (0.0039 min^{-1}) is higher than that of NST (0.00037 min^{-1}).

To explain such findings, the role of SiO_2 has to be taken in account. According to the N_2 physisorption measurements (Figure 7),[13,18] NST features a significantly larger surface area than the silica-free NT sample. Moreover, electrophoretic mobility measurements for NST afforded a zeta potential value of −30.7 mV (Figure S4), as expected for negatively charged materials.[73–75] These data explain the different adsorption capabilities of NST towards the cationic MB (80%) and anionic MO (10%) dyes, respectively, and its high dispersibility in water.

As far as the NST photoactivity is concerned, even taking in consideration the different textural features of NST and free-silica NT from the inspection of Figures 8A and 8B, it can be concluded that the presence of SiO_2 is irrelevant for the degradation of the cationic MB dye, while it was a determining factor for the degradation of anionic MO. It was already reported that the photocatalytic effectiveness of SiO_2@TiO_2 nanocomposites is the result of the synergistic interplay between adsorption/diffusion processes of dyes, taking place on the catalyst surface and the photoactivity of the TiO_2 component. In general, SiO_2 drives the adsorption of cationic and TiO_2 that of anionic dyes.[76,77] Such a cooperative effect seems to be operating in the UV degradation process of MO, where NST results more active than NT.[13,18] The same effect was not observed for MB, it being strongly attached to the photocatalyst surface.

It is likewise known that the presence of SiO_2 determines the formation of small TiO_2 crystallites. These, depending on the dimensions and/or Ti–O–Si bond formation, may induce a blue shift in TiO_2 photoactivation.[68] This explains the low NST visible light-driven photoactivity of NST, despite the presence of nitrized-TiO_2 NPs.

3. Conclusion

As a part of our ongoing research aimed to obtain SiO_2@TiO_2 photocatalysts by using ammonium-functionalized POSS-ILs as source of silica, here we have reported on the successful synthesis of SiO_2@nitrized-TiO_2 nanocomposite (NST) through calcination/carbonization (400 °C) of TiO_2 "xerogel" with OctaAmmonium POSS®. The reaction, performed in acidic conditions, led to a SiO_2@TiO_2 nanocomposite consisting in an almost homogeneous dispersion of small TiO_2 crystallites in amorphous silica. This material features a highly negatively charged surface with an area of 406 m^2g^{-1}, inducing high dispersion capabilities in water and unusual adsorption properties versus the cationic MB dye. It is noteworthy that this procedure also involves the nitrization of the TiO_2 crystallites. This does not produce photoactivity in the visible region, attributable to quantum effects phenomena related to small TiO_2 NPs and to Si–O–Ti bond formation. The different photocatalytic behavior of NST, which results to be very efficient against MO and less so against MB, was attributed to the different contribution provided by the SiO_2 component on the overall photocatalytic degradation of the two dyes.

The herein proposed synthetic approach to SiO_2@TiO_2, based on the use of POSS-ammonium ILs, allows to operate a systematic modification of the starting reactions conditions, in terms of reactant ratio, order of the reactant addition, POSS-anion IL couple and so on. Studies are underway to ascertain how the nature of the POSS-ammonium ILs species[39–42,78] may influence the overall properties of the SiO_2@nitrized-TiO_2 and, hence, their photocatalytic and adsorption activities. These, in turn, depend on the combination of several factors such as quantum confinement effects, TiO_2/SiO_2 ratio, porosity, surface area, surface acid sites and, hence, pH. Moreover, the use of POSS-ammonium as a source of both silica and nitrogen-doping agent may represent an innovative and alternative route to VLA silica@N-doped TiO_2 mixed-oxide nanocomposites.[14,15,19]

In conclusion, the results of the present study constitute a good starting point to prepare SiO_2@nitrized-TiO_2 nano-systems with enhanced properties and controlled morphologies.

Experimental Section

Materials

All chemicals are grade reagents and used without further purification. Titanium isopropyloxide (TTiP, Aldrich 97%), NH_4Cl (Aldrich 99%), methylene blue, methyl orange, deionized water, and absolute alcohol, were purchased from Sigma–Aldrich; OctaAmmonium POSS® was purchased from Hybrid Plastics.

Preparation

SiO_2@nitrized-TiO_2 Nanocomposite (NST)

The TiO_2 nanoparticle precursor was obtained by a conventional sol-gel process by using a molar ratio of 1:20:1:1 for TtiP:EtOH:HNO_3:H_2O. TTiP was dissolved in ethanol and the resulting solution left under stirring for ca. 30 min. Then, a 1:1:20 HNO_3/H_2O/EtOH solution was dropwise added to the alcoholic TTIP solution, and the resulting mixture left under power ultrasonic agitation for 15 minutes and then under stirring for 1 h. After this time, an aqueous solution of N-POSS (1/8 molar ratio with respect to TTiP) was added to afford a homogeneous suspension, which was left under stirring overnight and then on standing in a Petri

dish for 24 h. The curing process was performed at 100 °C for 48 h thus producing N-POSS@TiO_2 as a white solid. The calcination performed at 400 °C for 5 h in air (2 °C min^{-1} heating rate) afforded NST as a light beige solid. Elemental composition [%]: N 5.2, O 74.9, Si 8.0, Ti 11.9.

N-Doped TiO_2 (NT)

Silica free N-doped TiO_2 was prepared in the same experimental conditions as NST, by using NH_4Cl as N-doping agent. Elemental composition [%]: N 7.2, O 70.0, Ti 22.8.

Characterization

X-ray diffraction analysis was performed by a Bruker D_2 Phaser desktop diffractometer equipped with a Cu tube ($\lambda = 1.54056$ Å), recording the data in the 10°–90° 2θ range, with an angular step size of 0.025° s^{-1}. The average crystallite size of all samples was calculated using the Scherrer formula [Eq. (4)]:

$$d = \frac{K\lambda}{\beta cos\theta} \quad (4)$$

where d represents the grain size; $K = 1$ is the Scherrer constant related to the shape and index (hkl) of the crystals; λ is the wavelength of the X-ray (Cu K_α, 1.54056 Å); θ is the diffraction angle of the peak; β stands for the full width at half-height of the peaks (in radians).

Micro-Raman measurements were performed by means of a NT-MDT Integra Spectra C, equipped with a MS3504i 350 mm monochromator. A DPSS laser operating at 532 nm (2.33 eV) was used as exciting source. A high numerical aperture objective (Mitutoyo, magnification 100X NA = 0.75) was used both to focus the laser beam on the sample surface and collect the scattered light from the sample. The collected light was dispersed by 600 lines mm^{-1} grating and detected by a cooled CCD camera (ANDOR Idus). A very low laser power (250 μW at the sample surface) has been used to avoid any local heating of the samples and annealing effects. The spatial homogeneity of the samples has been further taken into account by recording spectra from several random positions on each specimen and finally averaging the data in order to have a reliable picture of the entire sample. Then, they were analyzed using a commercially available spectroscopic analysis software package.

Morphological analysis of the synthesized NST sample was carried out through a focused ion dual beam/scanning electron microscope (FIB-SEM Crossbeam 540, ZEISS). Furthermore, the elemental analysis was performed by energy dispersive spectroscopy (EDS) (Aztec Oxford) at 20 kV.

X-ray photoelectron spectra (XPS) were measured at 45° take-off angle relative to the surface plane with a PHI 5600 Multi Technique System (base pressure of the main chamber 1×10^{-8} Pa).[56,57] Samples were excited with Al Kα X-ray radiation using a pass energy of 5.85 eV. Structures due to the Kα satellite radiations were subtracted from the spectra prior to data processing. The XPS peak intensities were obtained after Shirley background removal.[56,57] The atomic concentration analysis was performed by taking into account the relevant atomic sensitivity factors. The instrumental energy resolution was ≤0.5 eV. Spectra calibration was achieved by fixing the main C 1s signal at 285.0 eV.[57]

Infrared transmittance spectra were recorded using a JASCO FT/IR-430 spectrometer in the 4000–400 cm^{-1} scan range, with an instrumental resolution of 4 cm^{-1} using KBr/sample mixtures.

Nitrogen isotherms at −196 °C were measured in a Quantachrome Autosorb iQ3 gas sorption analyzer, after degassing the samples under vacuum at 300 °C for 1 h to remove impurities. The Brunauer Emmett Teller method was applied to calculate the total surface area (S_{BET}) using the adsorption data of $0.01 < p/p_0 < 0.07$. Pore size distribution was calculated using the BJH model and the pore volume was measured at the single point at $p/p_0 = 0.99$.

Photocatalytic Activity Measurements

The UV-Vis absorption response of the samples was investigated by means of a Perkin-Elmer Lambda 2 UV-Vis spectrometer in the 190–1100 nm range. MO and MB, respectively, were used as probe species for the evaluation of the photocatalytic activities of the samples. A Xe lamp was used as a light source, selecting the wavelength by means of a monochromator (HORIBA Jobin Yvon model H10UV). The experiment was performed at $\lambda_{exc}^{UV} = 300$ nm (6.5 mW cm^{-2}) and $\lambda_{exc}^{Vis} = 550$ nm (11 mW cm^{-2}). In order to evaluate the photocatalytic performance of the samples, 0.06 mg of catalyst were dispersed in 40 mL of MB or MO aqueous $1 \cdot 10^{-5}$ M solutions. Before irradiation, the reaction mixtures were stirred in the dark for approximately 1 h to achieve adsorption-desorption equilibrium among the reactants. The photo-degradation was monitored by recording UV-Vis spectra at different irradiation times, by following the intensity variation of the MB and MO absorption bands at 662 nm and 475 nm, respectively.

Zeta potential measurements were performed by electrophoresis with a Zeta sizer 3000 instrument (Malvern Instruments) on a distilled water dispersion of NST.

Author Contributions

Antonino Gulino and Sandra Lo Schiavo conceived and designed the work. Sandra Lo Schiavo wrote the manuscript. Claudia Triolo performed the Raman measurement and data analysis. Zainab Dahrouch and Abdellatif Aaliti studied the photocatalytic activity.

Amani Khaskhoussi prepared SEM micrographs and EDX data. Luca Spitaleri collected Infrared and XPS data. Georgia Papanikolaou, Paola Lanzafame and Patrizia Primerano collected and analyzed XRD, BET and Z-potential data.

Funding: This research was partially funded by the financial contribution of the Italian Ministry of University and Research (MIUR) PON R&I 2014-2020 TETI project (ARS01_003339) and University of Catania, PIA.CE.RI. project 2020–2022.

Conflict of Interest

The authors declare no conflict of interest.

Keywords: mixed oxides · N–TiO_2 · photoactivity · POSS · SiO_2@TiO_2

[1] F. Fresno, R. Portela, S. Suàrez, J. Coronado, *J. Mater. Chem. A* **2014**, *2*, 2863–2884.
[2] X. Chen, S. Mao, *Chem. Rev.* **2007**, *107*, 2891–2959.

[3] Z. Luo, A. S. Poyraz, C. H. Kuo, R. Miao, Y. Meng, S. Y. Chen, T. Jiang, C. Wenos, S. L. Suib, *Chem. Mater.* **2015**, *27*, 6–17.
[4] J. Hu, S. Zhang, Y. Cao, H. Wang, H. Yu, F. Peng, *ACS Sustainable Chem. Eng.* **2018**, *6*, 10823–10832.
[5] J. Zhang, Q. Xu, Z. Feng, M. Li, C. Li, *Angew. Chem. Int. Ed.* **2008**, *47*, 1766–1769; *Angew. Chem.* **2008**, *120*, 1790–1793.
[6] R. Asahi, T. Morikawa, T. Ohwaki, K. Aoki, Y. Taga, *Science* **2001**, *293*, 269–271.
[7] M. Pelaez, N. T. Nolan, S. C. Pillai, M. K. Seery, P. Falaras, A. G. Kontos, P. S. M. Dunlop, J. W. J. Hamilton, J. A. Byrne, K. O'Shea, M. H. Entezari, D. D. A. Dionysiou, *Appl. Catal. B* **2012**, *125*, 331–349.
[8] N. Serpone, A. V. Emeline, V. N. Kuznetsov, V. K. Ryabchuk, *Environmentally Benign Photocatalysts, Applications of Titanium Oxide-based Materials,* Eds. M. Anpo, P. V. Kamat, Springer, New York, NY, **2010**, pp. 35–111.
[9] V. Etacheri, M. K. Seery, S. J. Hinder, S. C. Pillai, *Chem. Mater.* **2010**, *22*, 3843–3853.
[10] H. R. Jafry, M. V. Liga, Q. Li, A. R. Barron, *Environ. Sci. Technol.* **2011**, *45*, 1563–1568.
[11] M. Hirano, K. Ota, *J. Am. Ceram. Soc.* **2004**, 87, 1567–1570.
[12] S. Soltan, H. Jafari, S. Afshar, O. Zabihi, *Water Sci. Technol.* **2016**, *74*, 1689–1697.
[13] W. Dong, Y. Sun, Q. Ma, L. Zhu, W. Hua, X. Lu, G. Zhuang, S. Zhang, Z. Guo, D. Zhao, *J. Hazard. Mater.* **2012**, 229–230, 307–320.
[14] Y. D. Hou, X. C. Wang, L. Wu, X. F. Chen, Z. X. Ding, X. X. Wang, X. Z. Fu, *Chemosphere* **2008**, *72*, 414–421.
[15] B. K. Valmiki, S. Mavengere, J. S. Kim, *Appl. Surf. Sci.* **2019**, *491*, 60–66.
[16] H. Peréz, R. Miranda, Z. Saavedra-Leos, R. Zarraga, R. Alonso, E. Moctezuma, J. Martínez, *RSC Adv.* **2020**, *10*, 39580–39588.
[17] A. Rosales, A. Maury-Ramírez, R. Mejía-De Gutiérrez, C. Guzmán, K. EsquivCoating *ngs* **2018**, *8*, 120.
[18] G. Zaccariello, E. Moretti, L. Storaro, P. Riello, P. Canto, V. Gombac, T. Montini, E. Rodrıguez-Castellòn, A. Benedetti, *RSC Adv.* **2014**, *4*, 37826–37837.
[19] T. P. Ang, C. S. Toh, Y. F. Han, *J. Phys. Chem. C* **2009**, *113*, 10560–10567.
[20] N. V. Plechkova, K. R. Seddon, *Chem. Soc. Rev.* **2008**, *37*, 123–150.
[21] T. Welton, *Biophys. Rev. Lett.* **2008**, *10*, 691–706.
[22] T. Torimoto, T. Tsuda, K.-i. Okazaki, S. Kuwabata, *Adv. Mater.* **2010**, *22*, 1196–1221.
[23] A. Eftekhari, *Ionic Liquid Devices. Royal Society of Chemistry.* **2018**. Available online: https://pubs.rsc.org/en/content/ebook/978-1-78801-183-9.
[24] Z. Li, Z. Jia, Y. Luan, T. Mu, *Curr. Opin. Solid State Mater. Sci.* **2008**, *12*, 1–8.
[25] H. Zhang, K. Dasbiswas, N. B. Ludwig, G. Han, B. Lee, S. Vaikuntanathan, D. V. Talapin, *Nature* **2017**, *542*, 328–331.
[26] J. C. Riedl, M. A. Akhavan Kazemi, F. Cousin, E. Dubois, S. Fantini, S. Loïs, R. Perzynski, V. Peyre, *Nanoscale Adv.* **2020**, *2*, 1560–1572.
[27] J. N. Pendleton, B. F. Gilmore, *Int. J. Antimicrob. Agents* **2015**, *46*, 131–139.
[28] K. S. Egorova, E. G. Gordeev, V. P. Ananikov, *Chem. Rev.* **2017**, *117*, 7132–7189.
[29] S. Lo Schiavo, F. De Leo, C. Urzì, *Appl. Sci.* **2020**, *10*, 6568.
[30] F. De Leo, A. Marchetta, G. Capillo, A. Germanà, P. Primerano, S. Lo Schiavo, C. Urzì, *Coating* **2021**, *11*, 26–46.
[31] M. Paszkiewicz-Gawron, M. MartaDługokęçka, L. Wojciech, M. C. Paganini, E. Giamello, T. Klimczuk, M. Paszkiewicz, E. Grabowska, A. Zaleska-Medynska, J. Łuczak, *ACS Sustainable Chem. Eng.* **2018**, *6*, 3927–3937.
[32] A. Rybinska-Fryca, A. Mikolajczyk, J. Łuczak, M. Paszkiewicz-Gawron, M. Paszkiewicz, A. Zaleska-Medynska, T. Puzyn *J. Colloid Interface Sci.* **2020**, *572*, 396–407.
[33] N. Kaur, V. Singh, *New J. Chem.* **2017**, *41*, 2844–2868.
[34] P. Cardiano, G. Lazzara, S. Manickam, P. Mineo, S. Milioto, S. Lo Schiavo, *Eur. J. Inorg. Chem.* **2012**, *34*, 5668–5676.
[35] S. Manickam, P. Cardiano, G. P. Mineo, S. Lo Schiavo, *Eur. J. Inorg. Chem.* **2014**, *16*, 2704–2710.
[36] M. A. Castriciano, N. Leone, P. Cardiano, S. Manickam, L. Monsù Scolaro, S. Lo Schiavo, *J. Mater. Chem. C* **2013**, *1*, 4746–4753.
[37] P. Cardiano, E. Fazio, G. Lazzara, S. Manickam, S. Milioto, F. Neri, G. P. Mineo, A. Piperno, S. Lo Schiavo, *Carbon* **2015**, *86*, 325–337.
[38] S. Lo Schiavo, P. Mineo, P. Cardiano, P. Piraino, *Eur. Polym. J.* **2007**, *43*, 4898–4904.
[39] K. Tanaka, Y. Chujo, *J. Mater. Chem.* **2012**, *22*, 1733–1746.
[40] H. Zhou, Q. Ye, J. Xu, *Mater. Chem. Front.* **2017**, *1*, 212–230.
[41] H. Ghanbari, B. G. Cousins, A. M. A Seifalian, *Macromol. Rapid Commun.* **2011**, *32*, 1032–1046.
[42] X. Chen, L. F. Dumée, *Adv. Eng. Mater.* **2019**, *21*, 1800667.
[43] F. Zhang, D. Sun, C. Yu, Y. Yin, H. Dai, G. Shao, *New J. Chem.* **2015**, *39*, 3065–3070.
[44] J. Łuczak, M. Marta Paszkiewicz, A. Krukowska, A. Malankowska, A. Zaleska-Medynska, *Adv. Colloid Interface Sci.* **2016**, *230*, 13–28.
[45] J. Łuczak, M. Marta Paszkiewicz, A. Krukowska, A. Malankowska, A. Zaleska-Medynska, *Adv. Colloid Interface Sci.* **2016**, *227*, 1–52.
[46] T. Ohno, K. Sarukawa, K. Tokieda, M. Matsumura, *J. Catal.* **2001**, *203*, 82–86.
[47] G. Zu, J. Shen, W. Wang, L. Zou, Y. Lian, Z. Zhang, *ACS Appl. Mater. Interfaces.* **2015**, *7*, 5400–5409.
[48] Z. Dingg, G. Q. Lu, P. F. Greenfield, *J. Phys. Chem. B* **2000**, *104*, 19, 4815–4820.
[49] O. Frank, M. Zukalova, B. Laskova, J. Kürti, J. Koltai, L. Kavan, *Phys. Chem. Chem. Phys.* **2012**, *14*, 14567–14572.
[50] E. J. Ekoi, A. Gowen, R. Dorrepaal, D. P. Dowling, *Results Phys.* **2019**, *12*, 1574–1585.
[51] A. Fujishima, X. Zhang, D. A. Tryk, *Surf. Sci. Rep.* **2008**, *63*, 515–582.
[52] G. Sivalingam, K. Nagaveni, M. S. Hegde, G. Madras, *Appl. Catal. B* **2003**, *45*, 23–38.
[53] J. C. Phillips, *Phys. Rev. B* **1987**, *35*, 6409–6413.
[54] Y. D. Glinka, M. Jaroniec, *J. Phys. Chem. B* **1997**, *101*, 8832–8835.
[55] T. Uchino, Y. Tokuda, T. Yoko, *Phys. Rev. B* **1998**, *58*, 5322–5328.
[56] A. Gulino, *Anal. Bioanal. Chem.* **2013**, *405*, 1479–1495.
[57] D. Briggs, J. T. Grant, *Surface Analysis by Auger and X-Ray Photoelectron Spectroscopy*, IMPublications, Chichester, UK, **2003**.
[58] Y. J. Jin, J. Linghu, J. Chai, C. S. Chua, L. M. Wong, Y. P. Feng, M. Yang, *S, J. Phys. Chem. C* **2018**, *122*,16600–16606.
[59] D. S. Bhachu, R. G. Egdell, G. Sankar, C. J. Carmalt, I. P. Parkin, *J. Mater. Chem. C* **2017**, *5*, 9694–9701.
[60] A. Gulino, G. G. Condorelli, P. G. Mineo, I. Fragalà, *Nanotechnology* **2005**, *16*, 2170–217.
[61] J. Wang, D. N. Tafen, J. P. Lewis, Z. Hong, A. Manivannan, M. Zhi, M. Li, N. Wu, *J. Am. Chem. Soc.* **2009**, *131*, 12290–12297.
[62] A. Contino, G. Maccarrone, M. E. Fragalà, L. Spitaleri, A. Gulino, *Chem. Eur. J.* **2017**, *23*, 14937–14943.
[63] J. Choudhury, R. Kaminker, L. Motiei, G. de Ruiter, M. Morozov, F. Lupo, A. Gulino, M. E. van der Boom, *J. Am. Chem. Soc.* **2010**, 132, 9295–9297.
[64] R. Kaminker, L. Motiei, A. Gulino, I. Fragalà, L. J. W. Shimon, G. Evmenenko, P. Dutta, M. A. Iron, M. E. van der Boom Stepwise, *J. Am. Chem. Soc.* **2010**, *132*, 14554–14561.
[65] M. E. Mahmoud, G. M. Nabil, H. Abdel-Aal, N. A. Fekry, M. M. Osman, *ACS Sustainable Chem. Eng.* **2018**, *6*, 4564–4573.
[66] S. D. Delekar, A. G. Dhodamani, K. V. More, T. D. Dongale, R. K. Kamat, S. F. A. Acquah, N. S. Dalal, D. K. Panda, *ACS Omega* **2018**, *3*, 2743–2756.
[67] A. Fina, D. Tabuani, F. Carniato, A. Frache, E. Boccaleri, G. Camino, *Thermochim. Acta* **2006**, *440*, 36–42.
[68] L. Pinho, M. J. Mosquera, *Appl. Catal. B* **2013**, 134–135, 205–221.
[69] A. IR Mirabedini, M. Mirabedini, A. A. Babalou, S. Pazokifard, *Prog. Org. Coat.* **2011**, *72*, 453–460.
[70] M. Thommes, *Chem. Ing. Tech.* **2010**, *82*, 1059–1073.
[71] M. Hussain, R. Ceccarelli, D. L. Marchisio, D. Fino, N. Russo, F. Geobaldo, *Chem. Eng. J.* **2010**, *157*, 45–51.
[72] A. Nezamzadeh-Ejhied, H. Zabihi-Mobarakeh, *J. Ind. Eng. Chem.* **2014**, *20*, 1421–1431.
[73] R. Mishra, R. Malviya, P. K. Sharma, *J. Drug Delivery Ther.* **2014**, *4*, 33–40.
[74] Y. Liu, M. Tourbin, S. Lachaiz, P. Guiraud, *Ind. Eng. Chem. Res.* **2012**, *51*, 1853–1863.
[75] A. L. Costa, S. Ortelli, M. Blosi, S. Albonetti, A. Vaccari, M. Dondi, *Chem. Eng. J.* **2013**, *225*, 880–886.
[76] E. K. Radwan, C. H. Langford, G. Achari *R. Soc. Open Sci.* **2018**, *5*, 180918.
[77] J. Fernańdez-Catala, M. Sańchez-Rubio, M. Navlani-García, A. Berenguer-Murcia, D. Cazorla-Amoroś, *ACS Omega* **2020**, *5*, 31323–31331.
[78] A. Vasanthakumar, G. Redhi, R. M. Gengan, in *Fundamentals of Nanoparticles. Application of Ionic Liquids in Nanotechnology* (Eds. A. Barhoum, A. S. H. Makhlouf), Elsevier, **2018**, pp 371–400.

Manuscript received: June 29, 2021
Revised manuscript received: September 21, 2021